Form finding and structural analysis of actively bent timber grid shells

B. D'Amico *, A. Kermani, H. Zhang

Centre for Timber Engineering (CTE), School of Engineering and the Built Environment, Edinburgh Napier University, Edinburgh, UK

ABSTRACT

Grid shells are efficient structural systems covering large open spaces with relatively small amount of materials. Also, post forming techniques allow realization of geometrically complex (free-form) shapes by means of standard connection systems. However, due to complexity of the analysis–design process, they are rarely utilized in construction design. In this paper, a 'facilitating' numerical framework is introduced in which, for a given continuous reference shape, a geometrically similar discrete model is found by implementation of a six degree of freedom formulation of the Dynamic Relaxation method, to handle members bending and torsional stiffness. A grid cutting pattern algorithm is introduced, as well as methods to numerically simulate the double-layer construction technique and a novel (single-node) cylindrical joint model. The methods are extensively tested and validated on a range of structures, from 'simple' single-rod cases to more complex, actively bent, grid shell frameworks.

© 2014 Elsevier Ltd. All rights reserved.

1. Introduction

Free-form grid-shell structures can be formed by connecting short straight beam elements together into nodes thus converting a curved continuous surface in a faceted shell. From a geometrical point of view, the described process deals with complex connection systems: Each element converges to the node of the grid at a different angle, thus non-standard connections (and Computer-Aided Manufacturing process) become inevitable. A 'low-tech' method for building free-form structures using standard (bolted/ screwed) connection systems is by bending initially flat elastic rods, such as solid timber planks/laths, to form actual continuous curves. For timber grid shells made of continuous bending members, two sub-categories can be defined [1] differentiating on the geometric parameters assigned to generate a grid on a surface: If screwed laminated timber ribs are arranged following geodesic patterns (shortest curve on a surface for two given points) the planks composing the rib will only be subjected to torsion and bending around the weak axis [2] enhancing the 'allowable' width of the the plank's cross section. This technique was used for the construction of the Hannover Expo pavilion [3]. A different approach was adopted in the design of the Mannheim timber grid

shell for the Garden Festival [4]. In this case, it was assumed a constant distance (50 mm) between the consecutive nodes belonging to the same rib, which was built-up with two overlapping laths (double layer technique). Accordingly, the resulting mesh geometry of the grid shell did not follow the geodesic paths (thus, lateral bending occurs as well). However, this second design approach allowed the possibility of assembling the grid shell laid out flat (as a two-way mat of straight continuous rods) and eventually post forming it in a double curved geometry by imposing external displacements under the form of temporary crane-cable systems or adjustable scaffolding [5–7]. With the main grid eventually formed, additional bracing elements can be added to the system enhancing the in-plane shear stiffness of the equivalent shell (Fig. 1). The terms *post formed* [7,8], *actively* or *elastically bent* [9] are usually used to describe such kind of grid shell structures.

2. Simulating the forming process

Since the construction of the Mannheim grid shell, only rarely this (latter) technique has been used. According to Kelly et al: *'The reason for the apparent lack of enthusiasm may stem from the unique challenges associated with the design and formation process'* [10]. Indeed, in order to draw out the post-formed grid shape (and gain information on the internal stress fields) a geometrically non-linear analysis is required to simulate the forming process.

* Corresponding author. Tel.: +44 (0) 131 455 2249.
    E-mail addresses: bernardinodamico@gmail.com, b.d'amico@napier.ac.uk
(B. D'Amico), a.kermani@napier.ac.uk (A. Kermani), j.zhang@napier.ac.uk (H. Zhang).

Regardless of the adopted numerical algorithm, the analysis will require the definition of initial parameters to be performed:

- The flat mat geometry (cutting pattern).
- The displacements' vector (boundary conditions).

'To design the Downland grid-shell, physical modelling of the structure was a central element of the design process, which was used to determine the boundary condition for the form-finding model' [5]. The final position of the boundary nodes detected from the 1:30 scale model was used as target to the external imposed displacements and the mat's cutting pattern geometry was (a priori) established to have a rectangular shape. Clearly, any simulation of the forming process will always require the preliminary modelling of scale models.

2.1. A two-step analysis approach

Different authors [7,11–16] addressed the problem of defining purely numerical procedures to speeding up the design process of such structural systems where a built up mat of initially straight elastic rods (usually timber or fiber reinforced polymer) is bent to obtain a form-resistant grid shell structure. Among these, an interesting concept that comes out is that of performing a geometrically non-linear analysis involving the use of a supporting surface on which the mat is 'forced' to bend. In general, the form finding procedure contemplates two consecutive analysis steps where the stress field is generated at the completion of the first step and then is carried forward as *initial condition value* on the second one:

- An initially unstressed (flat) two-way mesh is pulled on the reference surface by means of external axial springs [15] or external applied forces [13]. Alternatively, the mesh is positioned directly on the surface and constrained to slide on it [14].
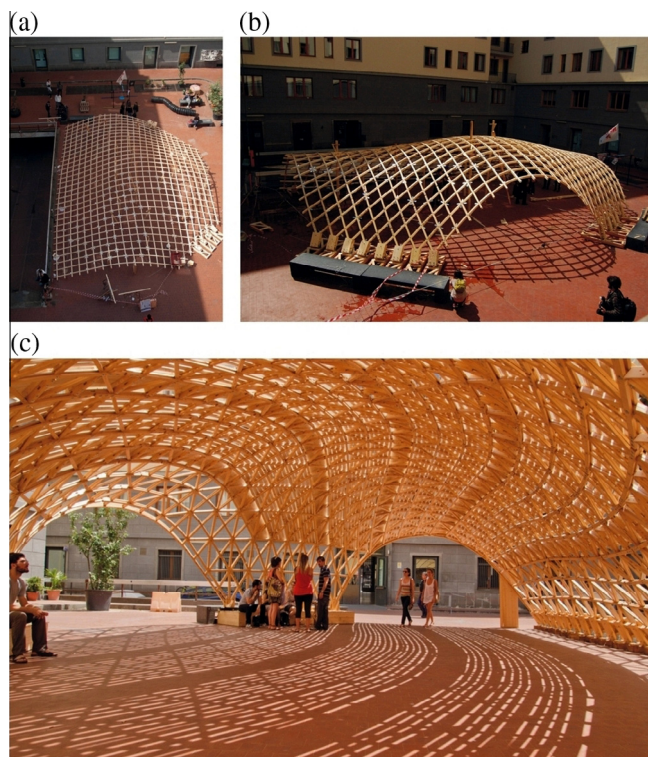
Fig. 1. Toledo timber grid shell in Naples, Italy 2012 [7]: (a) initial flat mat; (b) forming process; (c) complete structure.

- With the equilibrium shape found, the mesh geometry exceeding the reference surface is 'deleted' [15] (a cutting pattern is thus found) and translational degree of freedom (DoF) of the boundary nodes are constrained while previous external forces/constraints (shaping the net on the reference surface) are disabled/released, thus the system will assume a new equilibrium geometry, settling down to its final configuration.

Clearly, a two-step analysis scheme allows finding the equilibrium shape that is close to a reference surface which (acting basically as a form-work) can be modelled in accordance to a wide range of design requirements: Harris et al clearly explained how architectural and regulation parameters were driving the shape of the Pods grid shell roof and only in a second design phase '...a number of trials were made to establish a grid onto the surface' [17]. Moreover, with such approach there is no need for preliminary scale models since the mesh geometry (cutting pattern of the mat) and boundary conditions are obtained through the first analysis step.

3. Problem statement

Although information on methods involving the use of a reference surface can be found in literature [13–15,18] an effective description for a comprehensive numerical framework, and relative theoretical basis, seems still missing. The aim of the present study is to give a detailed description of the numerical implementation of the introduced methods.

4. Theory

4.1. The Dynamic Relaxation method

The DR is a fictitious time step marching scheme where, the position of the nodes representing the structural system is obtained by iterative numerical integration of the Newton's second law of motion until the entire system settles down in static equilibrium by application of a viscous or kinetic [19] damping term. The method was independently proposed by Day [20] for the analysis of prestressed concrete pressure vessels and Otter et al. [21] although (as noted by Topping and Khan [22]) its concept was already known by Rayleigh. The method has been extensively used for a wide range of structural problems with both geometric and material non-linearities as for instance, the form finding and load analysis of tension structures [23] where it provides more reliable results in terms of solution convergence if compared to the well known iterative matrix schemes with Newton–Raphson method [24]. Moreover, the DR does not require assembling/manipulation of a global stiffness matrix, hence it is relatively easy to implement and is highly suitable for parallel computing [22].

4.1.1. Rotational formulation with DR
The DR method is typically implemented by considering three DoF per node, where each link connecting two nodes can only simulate cable/strut behavior-like. In spite, it has been shown that three DoF schemes are able to simulate bending stiffness [25] if identical second moments of area, around any axis of the elements cross section, are provided. Further, torsional stiffness can be modelled as well by three DoF schemes if (in addition to cross section symmetry requirements) beams with a naturally curved (unstressed) shape are considered [26] and only small deflections are provided to occur. In order to provide a widely applicable method, not restricted to the aforementioned limitations, a more comprehensive Six DoF per node DR scheme (three translational DoF plus three rotational DoF) is here introduced.

Previous developments of beam elements with Six DoF and their resolution by DR schemes can be found in [27,28]. In these, the cross-section orientation is handled by introducing a third node for each beam element. A more refined approach (developed by Williams) [29] assumes a local reference frame for each node and a cubic shape function for the beam element in order to simulate axial, bending and torsional stiffness. The Six DoF DR theory introduced in the next subsection is based o this latter formulation.

4.2. Six DoF DR theory

Let us assume an elastic rod represented by a discrete list **P** of nodal coordinates $\bar{r}_i$ with arbitrary initial position in the Cartesian coordinate system:

$$\mathbf{P} = \{\bar{r}_i \ldots \bar{r}_n\}; \ \bar{r}_i = [x \quad y \quad z] \tag{1}$$

and a connectivity list **N** storing the nodes' indexes of the element ends $(1,2)$:

$$\mathbf{N} = \{n_j \ldots n_n\}; \ n_j = \{i_1, i_2\} \tag{2}$$

In addition, to the ith node is associated a local coordinate system $\{\bar{x}_i, \bar{y}_i, \bar{z}_i\}$ of unit vectors, with $\bar{z}_i$ the tangent direction to the rod's longitudinal axis and $\bar{x}_i, \bar{y}_i$ the cross sectional axes (see Fig. 2). Note that, as for the node position, the initial local system orientation can be arbitrary given.

4.2.1. Translations

Assuming a residual (out of balance) force $\bar{R}_i$ acting at the ith node as resultant of external applied loads $\bar{P}_i$ and internal reaction forces $\bar{F}_{prec.}$ and $\bar{F}_{succ.}$ of the elements preceding and succeeding the node:

$$\bar{R}_i = [R_{i,x} \quad R_{i,y} \quad R_{i,z}] = \bar{P}_i + \bar{F}_{prec.} + \bar{F}_{succ.} \tag{3}$$

and expressing the acceleration of node $\bar{r}_i$ at time t along the x direction according to Newton's second law of motion:

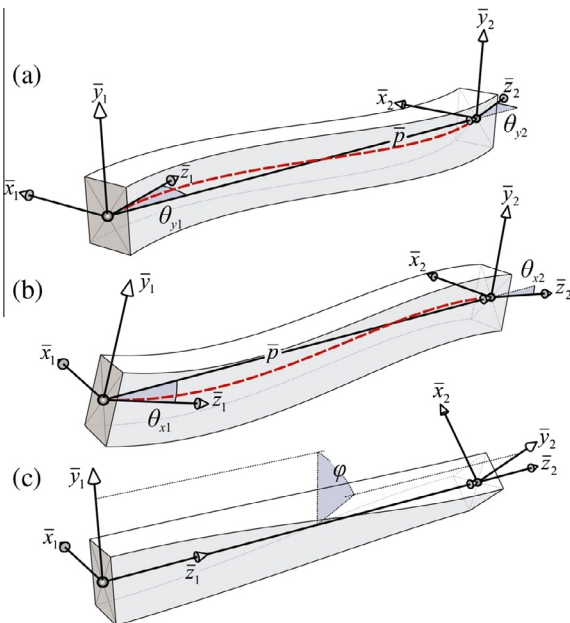$$\ddot{x}_i^t = \frac{R_{i,x}^t}{m_i} \tag{4}$$

Fig. 2. Element's local displacements according to the orientation of the ends' coordinate systems: (a) rotations around the local $\bar{y}$ axes; (b) rotations around the local $\bar{x}$ axes; (c) angle of twist; the dashed line represents the element's cubic shape function.

with m_i the fictitious [23] nodal mass, the updating velocity and displacement components are thus obtained by numerical integration of Eq. (4) which rearranged in a *velocity Verlet* scheme [30] gives the recurrence equation for the velocity term $\dot{x}_i$ at time t:

$$\dot{x}_i^t = C\dot{x}_i^{t-\Delta t} + \frac{\Delta t}{2}(\ddot{x}_i^{t-\Delta t} + \ddot{x}_i^t) \tag{5}$$

and the updated x_i coordinate projected at time $t + \Delta t$:

$$x_i^{t+\Delta t} = x_i^t + \dot{x}_i^t \Delta t + \frac{\Delta t^2}{2}\ddot{x}_i^t \tag{6}$$

where $C \in [0, 1]$ is a viscous damping term. At the first analysis iteration, the velocity term $\dot{x}_i^{t-\Delta t}$ and acceleration term $\ddot{x}_i^{t-\Delta t}$ of Eq. (5) can be set to zero. Repeating Eqs. (4)–(6) for the remaining y and z components of $\bar{R}_i$ for all the nodes of **P**, provides the updated geometry $\mathbf{P}^{t+\Delta t}$ to submit for the next DR iteration (to be run afterwards repositioning the constrained nodes).

The choice of an appropriate mass/time-increment ratio is of fundamental importance for DR analyses. Small lumped masses and a large time increment clearly reduce the number of iterations needed for equilibrium convergence, however, over a certain limit, numerical instability may occur. Another important parameter choice regards the value to assign for the viscous damping factor C, which should be proportional (for each node) to the fundamental modes of the system in order to avoid under (over) dumped vibrations, thus assuring fast equilibrium convergence. For an automatic assessment of the DR parameters see [31].

4.2.2. Rotations

Like for translations, a residual moment $\bar{H}_i$ is assumed at node $\bar{r}_i$ as the resultant of external applied moments $\bar{Q}_i$ and internal reaction moments $\bar{M}_{prec.}$, $\bar{M}_{succ.}$ of the two surrounding elements:

$$\bar{H}_i = [H_{i,x} \quad H_{i,y} \quad H_{i,z}] = \bar{Q}_i + \bar{M}_{prec.} + \bar{M}_{succ.} \tag{7}$$

Accordingly, the angular acceleration of node $\bar{r}_i$ around the Cartesian (global) x direction at time t is:

$$\ddot{\vartheta}_{i,x}^t = \frac{H_{i,x}^t}{\jmath_i} \tag{8}$$

where $\jmath_i$ is the fictitious lumped moment of inertia (or angular mass). Therefore, the recurrence equations of angular velocity $\dot{\vartheta}_i$ at time t and angle of rotation ϑ_i at time $t + \Delta t$ around the global x direction are:

$$\dot{\vartheta}_{i,x}^t = C\dot{\vartheta}_{i,x}^{t-\Delta t} + \frac{\Delta t}{2}(\ddot{\vartheta}_{i,x}^{t-\Delta t} + \ddot{\vartheta}_{i,x}^t) \tag{9}$$

$$\vartheta_{i,x}^{t+\Delta t} = \dot{\vartheta}_{i,x}^t \Delta t + \frac{\Delta t^2}{2}\ddot{\vartheta}_{i,x}^t \tag{10}$$

Noting that, while Eq. (6) provides an *absolute* coordinate value, the angle $\vartheta_{i,x}$ given by Eq. (10) is an *increment* of rotation (of the local coordinate system). Applying Eqs. (8)–(10) for the remaining components of $\bar{H}_i$ thus obtaining the rotation angles $\vartheta_{i,y}$ and $\vartheta_{i,z}$ around the Cartesian y and z directions; the local system orientation $\{\bar{x}_i, \bar{y}_i, \bar{z}_i\}^t$ is updated to $\{\bar{x}_i, \bar{y}_i, \bar{z}_i\}^{t+\Delta t}$ by pre-multiplying each unit vector with a rotation matrix $\widetilde{A}$ such that:

$$\bar{x}_i^{t+\Delta t} = \widetilde{A} \cdot \bar{x}_i^t \tag{11}$$

and $\widetilde{A}$ defined as:

$$\widetilde{A} = \widetilde{I}\cos\alpha + \widetilde{V}\sin\alpha + \widetilde{V}^2(1 - \cos\alpha) \tag{12}$$

where $\widetilde{I}$ is a 3×3 Identity matrix and $\widetilde{V}$ a Skew-symmetric matrix:

$$\widetilde{V} = \begin{bmatrix} 0 & -v_z & v_y \\ v_z & 0 & -v_x \\ -v_y & v_x & 0 \end{bmatrix} \tag{13}$$

Eq. (12) is a matrix form of the *Rodrigues' rotation formula* [32] to spatially rotate a vector ($\bar{x}_i^t$) around an axis (defined by the unit vector $\bar{v}$) by a given angle (α). As proposed by Williams (see Ref. [29]) the values of $\bar{v}$ and α can be obtained from the found rotation angles by using the *non-linear vector product* [33]. Assuming $\bar{x}, \bar{y}$ and $\bar{z}$ the unit vectors of the Cartesian space:

$$\bar{x} = [1 \quad 0 \quad 0]; \ \bar{y} = [0 \quad 1 \quad 0]; \ \bar{z} = [0 \quad 0 \quad 1] \tag{14}$$

and indicating with $\otimes$ the *non-linear vector product* operator, the rotation axis is obtained by the following expression:

$$\bar{a} = \left[\bar{x} \left(\tan \frac{\vartheta_{i,x}}{2} \right) \right] \otimes \left[\bar{y} \left(\tan \frac{\vartheta_{i,y}}{2} \right) \right] \otimes \left[\bar{z} \left(\tan \frac{\vartheta_{i,z}}{2} \right) \right] \tag{15}$$

Accordingly, the non-zero entries of $\widetilde{V}$ and rotation angle α needed to apply Eq. (12) are given by:

$$\bar{v} = \frac{\bar{a}}{|\bar{a}|}; \ \alpha = \arctan(2|\bar{a}|) \tag{16}$$

With the rotation matrix $\widetilde{A}$ thus determined, Eq. (11) can be applied for the remaining unit vectors $\bar{y}_i$ and $\bar{z}_i$ of the local coordinate system.

4.2.3. Computing residuals

In order to operate the described procedure, the out of balance forces $\bar{R}_i$ and moments $\bar{H}_i$ need to be computed at each time increment. For load analyses, the system of external applied loads is (a priori) known, while it will be set to null in case of form finding analyses. Therefore, only the reaction components in Eqs. (3) and (7) need to be computed. These vector quantities (expressed in the global coordinate system) acting on the ith node, can be obtained from the scalar force/moment reactions at the extremities of the elements surrounding $\bar{r}_i$. In turn, such (local) force and moment reactions are obtained from the local element displacements: With reference to Fig. 2 the rotations $\theta_{x,1}$, $\theta_{y,1}$, $\theta_{x,2}$, $\theta_{y,2}$ around the local $\bar{x}_1$, $\bar{y}_1$, $\bar{x}_2$, $\bar{y}_2$ axes; the angle of twist φ and the axial shortening/elongation of the generic n_j element are assumed to be:

$$\theta_{x,1} = \frac{\bar{y}_1 \cdot \bar{p}}{|\bar{p}|}; \ \theta_{y,1} = -\frac{\bar{x}_1 \cdot \bar{p}}{|\bar{p}|}; \ \theta_{x,2} = \frac{\bar{y}_2 \cdot \bar{p}}{|\bar{p}|}; \ \theta_{y,2} = -\frac{\bar{x}_2 \cdot \bar{p}}{|\bar{p}|} \tag{17}$$

$$\varphi = \frac{\bar{x}_1 \cdot \bar{y}_2 - \bar{x}_2 \cdot \bar{y}_1}{2} \tag{18}$$

$$e = \frac{|\bar{p}|^2 - L_0^2}{2L_0} + \frac{L_0}{60} \left[4 \left(\theta_{x,1}^2 + \theta_{y,1}^2 \right) - 2 \left(\theta_{x,1}\theta_{x,2} - \theta_{y,1}\theta_{y,2} \right) + 4 \left(\theta_{x,2}^2 + \theta_{y,2}^2 \right) \right] \tag{19}$$

with $\bar{p}$ the vector connecting the end nodes $\bar{r}_1$, $\bar{r}_2$ at time t and L_0 the unstressed length of the element (which may not correspond to the initial length). Differentiating the beam's expression of total strain energy U with respect to the found displacements, and indicating with A, I_x, I_y, J, E and G respectively: Cross sectional area, moments of area, torsional constant, Young's and shear modulus, the resulting element ends reactions are:

$$N = \frac{EA}{L_0} e; \ M_\varphi = \frac{GJ}{L_0} \varphi \tag{20}$$

$$M_{x,1} = \frac{NL_0}{30} (4\theta_{x,1} - \theta_{x,2}) + \frac{2EI_x}{L_0} (2\theta_{x,1} + \theta_{x,2}) \tag{21}$$

$$M_{x,2} = \frac{NL_0}{30} (4\theta_{x,2} - \theta_{x,1}) + \frac{2EI_x}{L_0} (2\theta_{x,2} + \theta_{x,1}) \tag{22}$$

$$M_{y,1} = \frac{NL_0}{30} (4\theta_{y,1} - \theta_{y,2}) + \frac{2EI_y}{L_0} (2\theta_{y,1} + \theta_{y,2}) \tag{23}$$

$$M_{y,2} = \frac{NL_0}{30} (4\theta_{y,2} - \theta_{y,1}) + \frac{2EI_y}{L_0} (2\theta_{y,2} + \theta_{y,1}) \tag{24}$$

where N is the internal axial force, M_φ the torsion moment around $\bar{p}$ and $M_{x,1}$, $M_{x,2}$, $M_{y,1}$, $M_{y,2}$ the bending moments about the $\bar{x}_1$, $\bar{x}_2$, $\bar{y}_1$, $\bar{y}_2$ local axes.

For a derivation of Eqs. (17)–(24) the reader is referred to Ref. [29]. It is only worth here to note that the coupling between translations and rotations is taken into account: In Eq. (19) the total shortening/elongation is obtained as summation of the element's axial deformation plus the contribution caused by element bowing (the first and second terms of the expression, respectively). This leads to the appearance of the axial force term N in Eqs. (21)–(24) taking into account the amount of moment generated by an axial force acting on a bent member. The local force-displacement relations for the jth element (Eqs. (20)–(24)) may be written in matrix form:

$$\mathbf{f} = \{\mathbf{K}_A^t + \mathbf{K}_B\} \cdot \mathbf{d} \tag{25}$$

where

$$\mathbf{f} = \begin{bmatrix} N \\ M_{x,1} \\ M_{x,2} \\ M_{y,1} \\ M_{y,2} \\ M_\varphi \end{bmatrix}; \ \mathbf{d} = \begin{bmatrix} 1 \\ \theta_{x,1} \\ \theta_{x,2} \\ \theta_{y,1} \\ \theta_{y,2} \\ \varphi \end{bmatrix} \tag{26}$$

$$\mathbf{K}_A^t = EAe \begin{bmatrix} 1/L_0 & 0 & 0 & 0 & 0 & 0 \\ 0 & 2/15 & -1/30 & 0 & 0 & 0 \\ 0 & -1/30 & 2/15 & 0 & 0 & 0 \\ 0 & 0 & 0 & 2/15 & -1/30 & 0 \\ 0 & 0 & 0 & -1/30 & 2/15 & 0 \\ 0 & 0 & 0 & 0 & 0 & 0 \end{bmatrix} \tag{27}$$

$$\mathbf{K}_B = \frac{1}{L_0} \begin{bmatrix} 0 & 0 & 0 & 0 & 0 & 0 \\ 0 & 4EI_x & 2EI_x & 0 & 0 & 0 \\ 0 & 2EI_x & 4EI_x & 0 & 0 & 0 \\ 0 & 0 & 0 & 4EI_y & 2EI_y & 0 \\ 0 & 0 & 0 & 2EI_y & 4EI_y & 0 \\ 0 & 0 & 0 & 0 & 0 & GJ \end{bmatrix} \tag{28}$$

As it can be seen, the stiffness matrix $\mathbf{K}_B$ only depends on the material properties and unstressed beam geometry, while $\mathbf{K}_A$ takes into account, at each time increment, the stiffness contribution due to element's shortening/elongation and bowing (e).

The nodal vector forces $\bar{F}_1$, $\bar{F}_2$ and moments $\bar{M}_1$, $\bar{M}_2$ generated by the above scalar quantities are:

$$\bar{F}_1 = \frac{N}{|\bar{p}|} \bar{p} + \bar{T}; \ \bar{F}_2 = -\bar{F}_1 \tag{29}$$

$$\bar{M}_1 = \bar{x}_1 M_{x,1} + \bar{y}_1 M_{y,1} + \bar{z}_1 M_\varphi \tag{30}$$

$$\bar{M}_2 = \bar{x}_2 M_{x,2} + \bar{y}_2 M_{y,2} - \bar{z}_2 M_\varphi \tag{31}$$

The shear force $\bar{T}$ in Eq. (29) can be found by imposing the equilibrium to rotation of the element: The resultant moment ($\bar{M}_1 + \bar{M}_2$) acting on the element, will generates a shear force oriented in the $\bar{u}$ direction orthogonal to both $\bar{p}$ and ($\bar{M}_1 + \bar{M}_2$) itself (see Fig. 3). Accordingly:

$$\bar{u} = \frac{(\bar{M}_1 + \bar{M}_2) \times \bar{p}}{|(\bar{M}_1 + \bar{M}_2) \times \bar{p}|} \tag{32}$$

The scaling value $|\bar{T}|$ of $\bar{u}$ to obtain $\bar{T}$ is given by the torque lever-arm relation:

$$|\bar{T}| = \frac{|\bar{M}_1 + \bar{M}_2|}{d}; \ d = |\bar{p}| \cdot \cos \eta \tag{33}$$

where $\cos \eta$ can be found by dot product between ($\bar{M}_1 + \bar{M}_2$) and a vector lying on the dashed line shown in Fig. 3, orthogonal to both $\bar{p}$ and $\bar{u}$:

$$\cos\eta = \frac{(\overline{M}_1 + \overline{M}_2) \cdot (\bar{p} \times \bar{u})}{|\overline{M}_1 + \overline{M}_2||\bar{p} \times \bar{u}|} \tag{34}$$

Rearranging Eqs. (33) and (34) gives the following expression for shear force:

$$\overline{T} = \bar{u}\frac{|\overline{M}_1 + \overline{M}_2|^2|\bar{p} \times \bar{u}|}{|\bar{p}|[(\overline{M}_1 + \overline{M}_2) \cdot (\bar{p} \times \bar{u})]} \tag{35}$$

4.3. Application of DR to elastic grid shells

4.3.1. Modelling cylindrical joints

In order to apply the previously described DR method for an actively bent grid shell system, the kinematic of the nodal connection need to be properly modelled. For a double layer grid shell, standard connections such as slotted-hole (Fig. 4) or clamping plate [34] systems may be provided. Alternatively, only one grid layer is pre-assembled and formed, thus the second layer is screwed on the previous one (lath by lath) in a second construction phase (e.g.: Savill garden grid shell construction [6]). In any of the aforementioned cases, a hinge mechanism will occur at the nodal connections of the two-way mat. In general, such hinge-like connections are numerically modelled by placing the mesh elements on two staggered levels and connecting them by means of *link* elements which allow rotation around their longitudinal axis. Although faithful to the real geometry, doubling the mesh nodes at each connection generates local eccentricities. On the contrary, a 'simpler' model with only one node per connection is numerically more stable. Such single-node model can be implemented by assuming a double connectivity list (**N**; **M** for instance) thus having two separate lists (Fig. 4b) one for each direction of the quadrangular mesh:

$$\mathbf{M} = \{m_k \dots m_n\}; \; m_k = \{i_1, i_2\} \tag{36}$$

and a second local coordinate system such that each connection is defined by a single position vector $\bar{r}_i$ but two local systems:

$$\{\bar{x}_{i,n}, \bar{y}_{i,n}, \bar{z}_{i,n}\}; \; \{\bar{x}_{i,m}, \bar{y}_{i,m}, \bar{z}_{i,m}\} \tag{37}$$

Accordingly; the residual out of balance force $\overline{R}_i$ is obtained as the resultant of reactions of the four elements surrounding $\bar{r}_i$:

$$\overline{R}_i = \overline{P}_i + \overline{F}_{prec,n} + \overline{F}_{succ,n} + \overline{F}_{prec,m} + \overline{F}_{succ,m} \tag{38}$$

while the rotational DoFs can be nodally decoupled by computing two distinct out of balance moments:

$$\overline{H}_{i,n} = \overline{Q}_{i,n} + \overline{M}_{prec,n} + \overline{M}_{succ,n}; \; \overline{H}_{i,m} = \overline{Q}_{i,m} + \overline{M}_{prec,m} + \overline{M}_{succ,m} \tag{39}$$

The resulting kinematic mechanism of the described model resembles a spherical joint acting between two rods (n and m). In order to simulate a (more realistic) cylindrical joint behavior, with $\bar{y}_{i,n} \equiv \bar{y}_{i,m}$ coincident with the joint rotational axis, the resulting angle β between $\bar{y}_{i,n}$ and $\bar{y}_{i,m}$ at the end of the DR iteration,
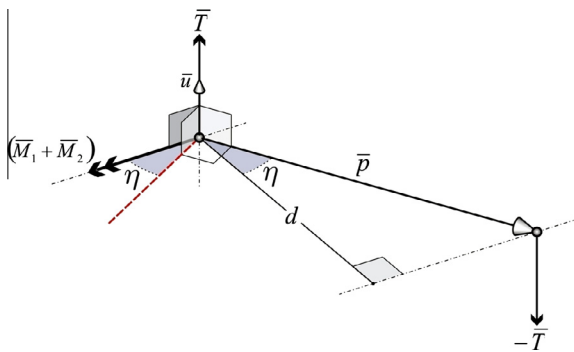

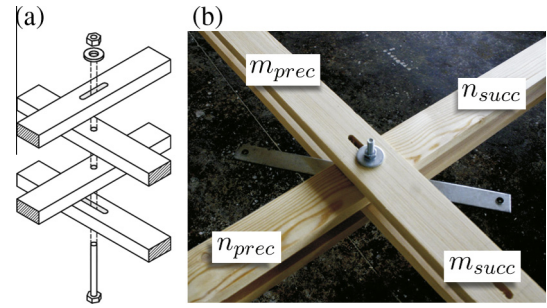**Fig. 3.** Shear reaction force $\overline{T}$ at the element's end nodes.

Fig. 4. Slotted hole connection system [4]: (a) schematic view; (b) two distinct **N** and **M** connectivity lists are used to define the equivalent numerical model.

has to be reset to zero (see Fig. 5). This task is performed by pre multiplying once more the local system orientations resulting from Eq. (11) with a rotation matrix Eq. (12) whose entries this time are given by:

$$\bar{v}^* = \frac{\bar{y}_{i,m} \times \bar{y}_{i,n}}{|\bar{y}_{i,m} \times \bar{y}_{i,n}|}; \; \alpha_n = \beta/2; \; \alpha_m = -\beta/2 \tag{40}$$

where α_n applies in Eq. (11) to rotate $\{\bar{x}_{i,n}, \bar{y}_{i,n}, \bar{z}_{i,n}\}$ and α_m applies to rotate $\{\bar{x}_{i,m}, \bar{y}_{i,m}, \bar{z}_{i,m}\}$. Of course, the local system orientations found by using Eqs. (40) do not correspond to an equilibrium configuration, as well as the nodes position at the current time anyway. Since we are only interested in the (final) static equilibrium configuration, the out of balance moment generated by the described 'artificial' rotation will gradually decrease with the residuals, eventually becoming small enough to be neglected (at analysis completion). Moreover, the described procedure allows semi-rigid behavior to be simulated as well (e.g. to take into account the connection stiffness) by scaling, at every time increment, the resulting α_n and α_m angles with a reducing factor $s \in [0, 1]$.

4.3.2. Modelling double layer systems

The double layer technique allows to obtain more tight curvatures compared to a single layer mat made of laths with equivalent cross sectional area. Then, at completion of the forming process, the sliding between overlapping laths is constrained (thus, enhancing the bending stiffness of the built-up rib) by inserting shear timber blocks in between the laths making up the single rib. Accordingly, for form finding analyses, the cross sectional area, and moments of area to assign in Eq. (25) can be assumed as double of the corresponding single lath values. In particular, according to Fig. 6, the moment of area I_x results to be:

$$I_x = bh^3/6 \tag{41}$$

Nevertheless, for load analyses, the increase of bending stiffness around the x axis for effect of the shear blocks, need to be taken into account: Assuming a rigid timber block (infinite transverse shear modulus) and a rigid laths-block connection interface, the resulting moment of area around the x local axis can be assumed as:

$$I_x = \frac{b(2h + h_s)^3}{12} - \frac{bh_s^3}{12} \tag{42}$$

with h_s the shear block height. On the opposite, assuming the stiffness contribution given by the shear blocks as null, the resulting I_x value is obviously that given by Eq. (41). On this basis, and assuming compatibility in the curvature and displacements of overlapping laths (hence, considering any shear flexibility of the composite section as null) a general equation can be arranged:

$$I_x = c_s\left(\frac{h^2}{2} + \frac{h_s^2}{2} + hh_s\right)bh + \frac{bh^3}{6}; \; c_s \in [0, 1] \tag{43}$$
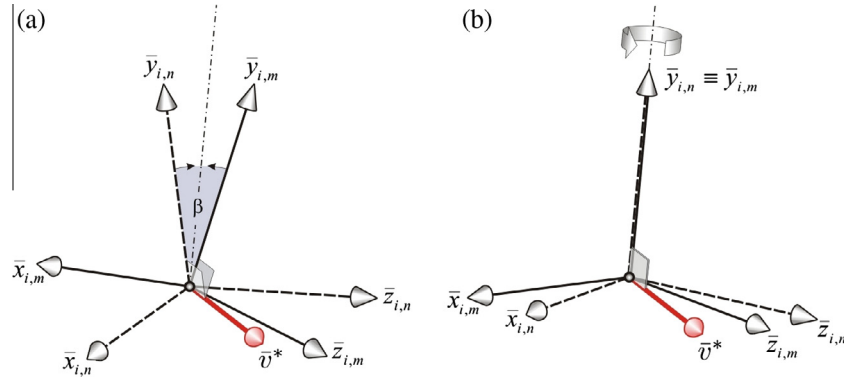
Fig. 5. Local coord. systems of the surrounding n and m elements at node i: (a) spherical hinge. The rotations of the two systems are decoupled; (b) cylindrical joint. The $\bar{y}_{i,n}$ and $\bar{y}_{i,m}$ local axes are constrained along the same direction.
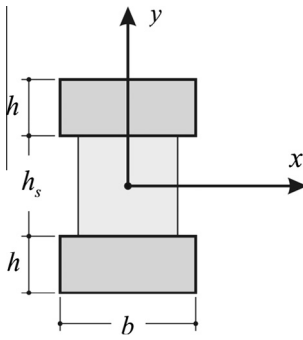

Fig. 6. Built-up cross section.

Accordingly, c_s is set to zero for form finding analyses, while a value $\neq 0$ is calibrated (e.g. by experimental bending tests) for load analyses in order to take into account the increase in bending stiffness due to the presence of shear blocks.

Of course, when setting the updated moment of area value for load analyses (at completion of the two-step form finding routine) the occurring change in stiffness will generate unbalancing forces. In other terms, the system will set in the equilibrium configuration that would result by forming the double layer mat with shear blocks already screwed on at the flat configuration. In order to maintain the equilibrium geometry obtained at form finding completion (with $I_x^{c_s=0}$) the corresponding element ends reactions $M_{x,1}, M_{x,2}$ must maintain the found equilibrium value ($M_{x,1}^{eq.}$, $M_{x,2}^{eq.}$) regardless of the new $I_x^{c_s\neq0}$ value. Therefore, the resulting angular displacements $\theta_{x,1}^{eq.}$ and $\theta_{x,2}^{eq.}$ in the second term of Eqs. (21) and (22) need to be multiplied with a reducing factor corresponding to the ratio ($I_x^{c_s=0}/I_x^{c_s\neq0}$):

$$M_{x,1}^{eq.} = \frac{NL_0}{30}(4\theta_{x,1}^{eq.} - \theta_{x,2}^{eq.}) + \frac{2EI_x^{c_s\neq0}}{L_0}\left[2\left(\frac{I_x^{c_s=0}}{I_x^{c_s\neq0}}\right)\theta_{x,1}^{eq.} + \left(\frac{I_x^{c_s=0}}{I_x^{c_s\neq0}}\right)\theta_{x,2}^{eq.}\right] \quad (44)$$

$$M_{x,2}^{eq.} = \frac{NL_0}{30}(4\theta_{x,2}^{eq.} - \theta_{x,1}^{eq.}) + \frac{2EI_x^{c_s\neq0}}{L_0}\left[2\left(\frac{I_x^{c_s=0}}{I_x^{c_s\neq0}}\right)\theta_{x,2}^{eq.} + \left(\frac{I_x^{c_s=0}}{I_x^{c_s\neq0}}\right)\theta_{x,1}^{eq.}\right] \quad (45)$$

The occurring difference values between the actual angular displacements and the reduced values are:

$$\theta_{x,1}^{eq.} - \left(\frac{I_x^{c_s=0}}{I_x^{c_s\neq0}}\right)\theta_{x,1}^{eq.}; \quad \theta_{x,2}^{eq.} - \left(\frac{I_x^{c_s=0}}{I_x^{c_s\neq0}}\right)\theta_{x,2}^{eq.} \quad (46)$$

From a physical point of view, such difference in values can be conceived as the unstressed residual angles that would result if we release the boundary constraints of the formed grid but leaving the

shear blocks inserted. It is easy to understand that, in doing such operation, the screwed double layer mat would not assume the flat geometry anymore. Accordingly, for a load analysis performed in continuity of a form finding analysis, the rotation angles around the local x axes measured at time t by Eqs. (17) have to be deduced of the quantity given by Eq. (46) thus, the force-displacement relations (21) and (22) become:

$$M_{x,1} = \frac{NL_0}{30}(4\theta_{x,1} - \theta_{x,2}) + \frac{2EI_x^{c_s\neq0}}{L_0}\left\{2\left[\theta_{x,1} - \theta_{x,1}^{eq.}\left(1 - \frac{I_x^{c_s=0}}{I_x^{c_s\neq0}}\right)\right]\right.$$
$$\left. + \left[\theta_{x,2} - \theta_{x,2}^{eq.}\left(1 - \frac{I_x^{c_s=0}}{I_x^{c_s\neq0}}\right)\right]\right\} \quad (47)$$

$$M_{x,2} = \frac{NL_0}{30}(4\theta_{x,2} - \theta_{x,1}) + \frac{2EI_x^{c_s\neq0}}{L_0}\left\{2\left[\theta_{x,2} - \theta_{x,2}^{eq.}\left(1 - \frac{I_x^{c_s=0}}{I_x^{c_s\neq0}}\right)\right]\right.$$
$$\left. + \left[\theta_{x,1} - \theta_{x,1}^{eq.}\left(1 - \frac{I_x^{c_s=0}}{I_x^{c_s\neq0}}\right)\right]\right\} \quad (48)$$

Thus, Eq. (25) can be rewritten as:

$$\mathbf{f} = \{\mathbf{K}_A^t + \mathbf{K}_B\} \cdot \mathbf{d} + \mathbf{K}_C \cdot \mathbf{d}^{eq.} \quad (49)$$

where

$$\mathbf{K}_C = \frac{2E}{L_0}\begin{bmatrix} 0 & 0 & 0 & 0 & 0 & 0 \\ 0 & 2(I_x^{c_s=0} - I_x^{c_s\neq0}) & (I_x^{c_s=0} - I_x^{c_s\neq0}) & 0 & 0 & 0 \\ 0 & (I_x^{c_s=0} - I_x^{c_s\neq0}) & 2(I_x^{c_s=0} - I_x^{c_s\neq0}) & 0 & 0 & 0 \\ 0 & 0 & 0 & 0 & 0 & 0 \\ 0 & 0 & 0 & 0 & 0 & 0 \\ 0 & 0 & 0 & 0 & 0 & 0 \end{bmatrix}; \mathbf{d}^{eq.} = \begin{bmatrix} 0 \\ \theta_{x,1}^{eq.} \\ \theta_{x,2}^{eq.} \\ 0 \\ 0 \\ 0 \end{bmatrix} \quad (50)$$

The non-null entries of $\mathbf{d}^{eq.}$ are obtained obviously at completion of the form finding analysis according to the resulting equilibrium geometry. The value of I_x in $\mathbf{K}_B$ is set to $I_x^{c_s=0}$ for the form finding routine while it is set to $I_x^{c_s\neq0}$ for the successive load analysis.

4.3.3. Surface constraints

Provided an appropriate mass/time-increment ratio, the DR methods will always converge to an equilibrium configuration of minimum strain energy (which is typical of explicit numerical schemes such as DR) no matter how gross is the deformation of the initial grid on the reference surface. Nonetheless, a mere random distribution of the initial nodes' position may results in a grid which will 'fold back' on itself on the reference surface at analysis

completion. A simple measure to prevent the analysis converging to such an equilibrium configuration of 'local' minimum strain energy, is assuring a 'certain' degree of geometric regularity for the initial grid pattern, which for instance, may be generated by projection maps (e.g. cartesian, gnomonic, cylindrical, spherical, etc.) from a matrix of point.

Clearly, fundamental requirement to generate the initial position of the nodes is obviously that they have to lie on the reference surface. Assuming the reference surface described by a *real* function of the kind $f(\bar{r}) = 0$ with $\bar{r}$ a coordinate vector defined in $\mathbb{R}^3$ (see Eq. (1)):

$$\mathbf{P} = \{\bar{r} | f(\bar{r}) = 0\} \tag{51}$$

In addition, we have to define a subspace of interest of the Cartesian space containing the part of mesh (a subset of $\mathbf{P}$) that we want constrained to slide on the surface. Indicating with $\mathbf{B} \subset \mathbb{R}^3$ the subspace of interest, in case the ith node falls into $\mathbf{B}$ ($\bar{r}_i \in \mathbf{B}$) then, only the tangent-to-surface component ($\overline{R}_{i\parallel}$) of the out-of-balance force ($\overline{R}_i$) is considered:

$$\overline{R}_{i\parallel} = \bar{w}_i \times (\overline{R}_i \times \bar{w}_i) \tag{52}$$

On the opposite, for $\bar{r}_i \notin \mathbf{B}$, the full residual obtained by Eq. (38) is inserted in Eq. (4) to eventually obtain the updated node position. The unit vector normal to the surface $\bar{w}_i$ appearing in Eq. (52) is given by [35]:

$$\bar{w}_i = \frac{\frac{\partial f}{\partial x}\bar{x} + \frac{\partial f}{\partial y}\bar{y} + \frac{\partial f}{\partial z}\bar{z}}{\sqrt{\left(\frac{\partial f}{\partial x}\right)^2 + \left(\frac{\partial f}{\partial y}\right)^2 + \left(\frac{\partial f}{\partial z}\right)^2}} \tag{53}$$

with x, y and z the components of $\bar{r}_i$, while $\bar{x}$, $\bar{y}$ and $\bar{z}$ are the unit vectors as defined in Eqs. (14). Even though, we constrained certain nodes to move along the tangent-to-surface direction, their updated node position (given by Eqs. (6)) will almost surely be off the surface: $f(\bar{r}_i) \neq 0$. Therefore, prior to running the next DR iteration, those nodes have to be pulled back on the surface. The closest coordinate position on the surface ($\bar{r}_i^*$) of the $\bar{r}_i$ node is given by [35]:

$$\bar{r}_i^* = \bar{r}_i - \frac{f(\bar{r}_i)\left[\frac{\partial f}{\partial x}\bar{x} + \frac{\partial f}{\partial y}\bar{y} + \frac{\partial f}{\partial z}\bar{z}\right]}{\left(\frac{\partial f}{\partial x}\right)^2 + \left(\frac{\partial f}{\partial y}\right)^2 + \left(\frac{\partial f}{\partial z}\right)^2} \tag{54}$$

As alternative to the computing of tangential residuals and node repositioning (Eqs. (52)–(54)) an external 'pulling' force $k(\bar{r}_i^* - \bar{r}_i)$ can be added in Eq. (38) to constrain the elastic grid moving close to the reference surface but allowing some clearance as well, in order to reduce the resulting bending stress. Such pulling force can be conceived as the effect of an axial spring linking each grid node $\bar{r}_i$ to the surface in $\bar{r}_i^*$. The spring stiffness k is calibrated to reduce/increase the clearance amplitude. Noting that (unlike in [15]) the surface node position $\bar{r}_i^*$ is recomputed at each time increment as the closest to $\bar{r}_i$ thus, the corresponding spring force will not induce any undesirable axial stress to the elastic grid during the forming simulation. Of course, a value of k varying for each node may be provided as well, in order to (smoothly) reduce the clearance in some areas, e.g. at the surface boundary.

4.3.4. Mesh cutting

Once the elastic grid constrained to the surface reaches a static equilibrium configuration, at completion of the first DR analysis step, the mesh geometry is initialized (thus submitted to the second analysis step) by 'cutting' the excess part. This task is performed by interrogating the connectivity lists $\mathbf{N}$ and $\mathbf{M}$ checking for each element, whether the corresponding end nodes fall into subspace $\mathbf{B}$, thus the connectivity lists are updated accordingly, discharging all the elements outside $\mathbf{B}$. However, if an element crosses the subspace of interest, manipulation of the geometry list $\mathbf{P}$ is required. In other terms, we need to find the nodal coordinates $\bar{r}_0$ at the point of intersection between the boundary of $\mathbf{B}$ and the element's shape function: Let assume that $\mathbf{B}$ is lower bounded by $z \geqslant 0$ and $\bar{r}(t)$ is the cubic *Hermite* shape function of the crossing element, defined by the end nodes coordinates ($\bar{r}_{i_1}$; $\bar{r}_{i_2}$) and tangent unit vectors ($\bar{z}_1$; $\bar{z}_2$) as shown in Fig. 2: The problem is reduced to find the value of t_0 such that $\bar{r}(t_0)$ lies on the global (x, y) plane:

$$t_0 \to \bar{r}(t_0) = [x \quad y \quad 0]; \ t_0 \in [0, 1] \tag{55}$$

hence we take into account only the third component of $\bar{r}$ in Eq. (55):

$$t_0 \to z(t_0) = 0 \tag{56}$$

The solution of the cubic function (56) may be analytically found (e.g. by Cardano's method or Vieta's substitution). Alternatively, an iterative method such us Newton–Raphson may be used:

$$t^{n+1} = t^n - \frac{z(t^n)}{\left(\frac{\partial z}{\partial t^n}\right)} \tag{57}$$

The value of t_0 so found is then inserted in the remaining two $x(t)$ and $y(t)$ of $\bar{r}(t)$ thus obtaining $\bar{r}_0$. Extending the problem to the general case of $\mathbf{B}$ bounded by a plane with arbitrary orientation, Eq. (56) becomes:

$$t_0 \to \bar{\omega}_p \cdot [\bar{r}(t_0) - \bar{r}_p] = 0 \tag{58}$$

with $\bar{\omega}_p$ the vector normal to the plane and $\bar{r}_p$ a point of the plane. Therefore, the recurrence Eq. (57) becomes:

$$t^{n+1} = t^n - \frac{\bar{\omega}_p \cdot [\bar{r}(t^n) - \bar{r}_p]}{\bar{\omega}_p \cdot \left(\frac{\partial \bar{r}}{\partial t^n}\right)} \tag{59}$$

The new boundary node so found is added to the node list $\mathbf{P}$ and the connectivity index of the crossing element is updated accordingly.

A description of the algorithm is given with reference to Fig. 7: The element '*12*' crosses the subspace with its *start* node 4 thus the new node 8 is computed and the element's connectivity is updated as shown in Fig. 7b while, element '*19*' remains connected to node 4. By adding a new node to the $\mathbf{P}$ geometry list rather updating the coordinate values of the former (start/end) node, there is no need for following any particular (geometric/spatial) order in inspecting the connectivity list, thus allowing parallel access and computing schemes.

5. Numerical tests

5.1. Elastica

As in [11,25] the described six DoF DR formulation is firstly tested, in the bi-dimensional case, against the analytical solution of an initially straight elastic rod pinned at its ends. Fig. 8 details the corresponding *Elastica* shapes for the effect of four increasing values of the axial load P over the critical Euler buckling value P_{cr}, identifying each shape with the corresponding inclination angle of the end's tangential direction. The load values of P corresponding to the four shapes, are obtained according to Timoshenko and Gere[1] as: $P = (K^2 \cdot EI)L^{-2}$ [36]. A bending stiffness $EI = 100$ kN m^2 and an axial stiffness $EA = 100$ MN were set. The rod's length is 10 m. For each of the four buckled states, five DR analyses with increasing number of elements (20, 24, 28, 32 and 36) were performed. The analyses were stopped when the following inequality limit was reached:

---

[1] The length L in [36] corresponds to $L/2$ of the present study; The *complete elliptic integral of the first kind* (K) has been calculated up to the 10th decimal place in order to maintain high accuracy of the analytic solution of P.
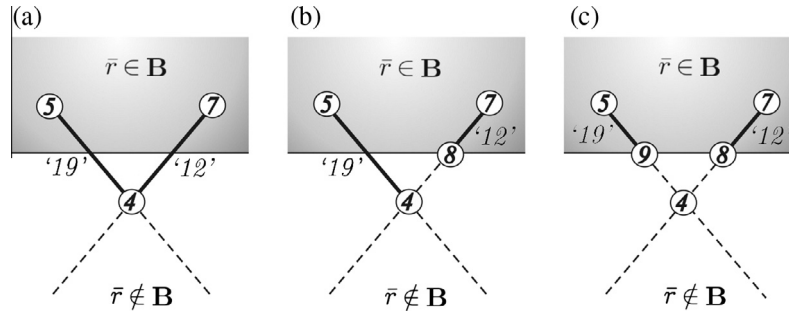
Fig. 7. Cutting algorithm: (a) two elements crossing the subspace **B** are connected to the same node 4; (b) at the 12th iteration the *end* node of element '12' is updated, while element '19' remains linked to node 4; (c) the boundary node 9 can be (independently) computed at the 19th iteration.
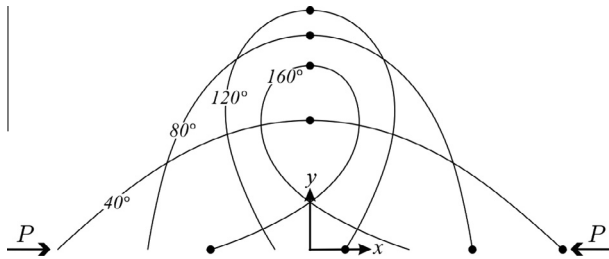

Fig. 8. *Elastica* shapes under four buckled states. The numerical *x* displacement and *y* displacement errors of the right-end and midspan nodes, are reported in Fig. 9.

Fig. 9. Numerical error of displacements at different discretization values for a buckled elastic rod (shown in Fig. 8).

$max \mid \overline{R}_i \mid \leqslant 9.5e - 6P$. The numerical *x* displacement of the rod's right-end node and *y* displacement of the mid-span node are compared to the corresponding analytical values in terms of error percentage and are summarized in Fig. 9.

$$x[\%] = \frac{100|x^A - x^{DR}|}{x^A}; \ y[\%] = \frac{100|y^A - y^{DR}|}{y^A} \qquad (60)$$

As expected, the numerical error is inversely proportional to the number of elements used to modelling the discrete rod. Higher error percentages are registered for the 40° buckled state, with a maximum error of 1.5% most probably due to axial deformation (not taken into account in the analytical solution) of the numerical model. Remarkably, the error of the 36 elements model, falls below the 0.5% for all four buckled configurations.

5.2. Combined bending and torsion

A further numerical test on the single rod case is performed to assess the reliability of the method in the three-dimensional case, involving combined bending moment and torsion effects: Firstly, a 10 m long rod is bent as in the previous test (dashed line in Fig. 10) until a distance between ends of 6.2 m is reached. Secondly, the rod is prevented from rotating around the global *x* axis at its end nodes and combinations of increasing forces $\overline{P}$ and constant torque $\overline{Q}$ are applied at the midspan node. The analyses described were then replicated with the commercial Finite Element software Abaqus with Newton–Raphson solver (NR), to handle *large displacements*. A 36-element geometry was set up for both NR and DR models, while the axial and bending stiffness was set in accordance to the previous test ($I_x = I_y = I$) as well as the convergence criteria. In addition, a torsional stiffness value $GJ = 50$ kN m² was assumed.

The resulting *y* and *z* displacements and rotation angle γ at the mid-span node, for five $\overline{P}$–$\overline{Q}$ load combinations, obtained with both NR and DR methods, are reported in Table 1. As can be seen, both methods give very close results, especially if we consider the magnitude of displacements involved. At load case **5** the mid-span
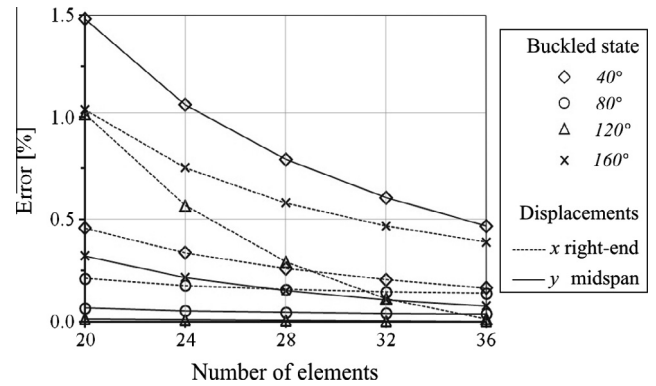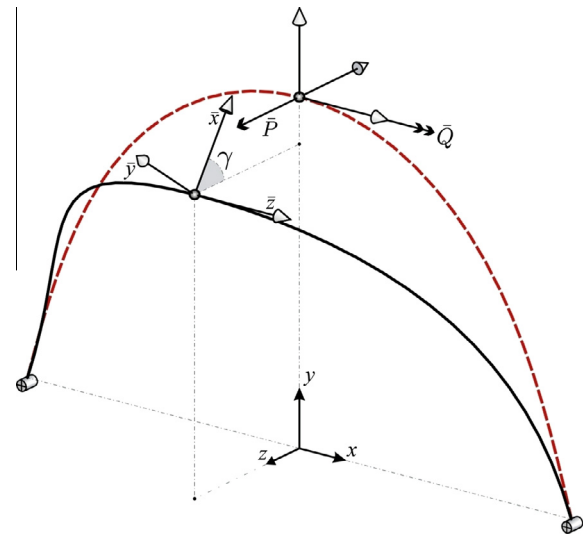

Fig. 10. Combined bending and torsion numerical tests set up: displacements *y*, *z* and rot. angle γ of the midspan node for different $\overline{P}$–$\overline{Q}$ values are reported in Table 1.

node achieves a lateral (*z*) displacement of more than 1.6 m with an occurring discrepancy between NR and DR analyses output of 0.9 cm (≈0.5%) and a difference between vertical (*y*) components of 0.5 cm on a total value of almost 3 m (≈0.16%). Not least, the rod's cross section at the midspan node undergoes a rotation γ of 0.942 rad (circa 54°) corresponding to a gap of only 0.0052 rad (0.3°) between NR and DR outputs (≈0.5%). For completeness of results, the bending reactions M_x, M_y at the elements midpoint and torsion M_φ (second of Eqs. (20)) outputs of the DR analyses

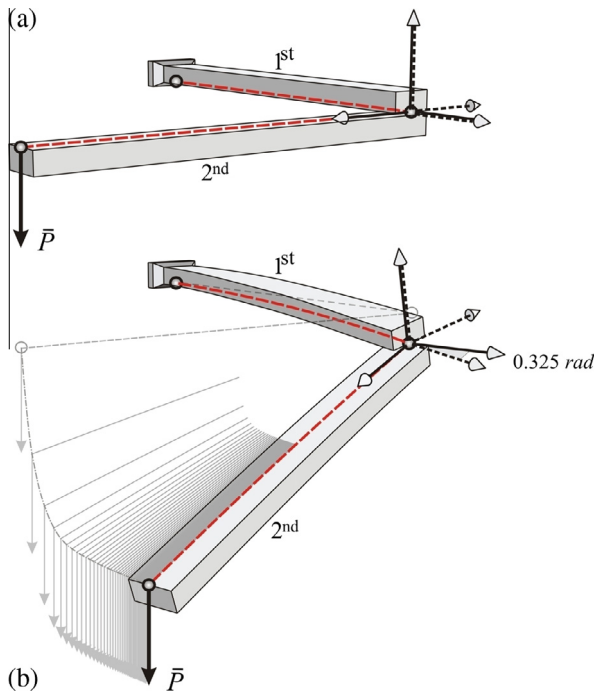**Table 1**
NR and DR methods: comparison of displacement values at the midspan node of a pre-stressed rod under five load combinations (see Fig. 10).

Load case	1		2		3		4		5	
P (kN)	0.0		5.0		10.0		15.0		20.0	
Q (kN m)	10.0		10.0		10.0		10.0		10.0	
	NR	DR	NR	DR	NR	DR	NR	DR	NR	DR
y/L^a	0.3421	0.3420	0.3357	0.3359	0.3251	0.3255	0.3119	0.3124	0.2975	0.2980
z/L	0.0239	0.0235	0.0656	0.0645	0.1032	0.1018	0.1358	0.1344	0.1633	0.1621
γ (rad)	0.5646	0.5664	0.6807	0.6789	0.7856	0.7814	0.8754	0.8701	0.9498	0.9442

 ^{a} L = 10.0 m.

Table 2
NR and DR methods: comparison of internal reactions, measured at the elements midpoint, under the $(\overline{P}\text{-}\overline{Q})$ load case **2**.

Elem. internal reaction (kN m)	M_x		M_y		M_φ	
Elem. index	NR	DR	NR	DR	NR	DR
1	1.12	1.14	−33.65	−33.38	5.03	5.00
6	13.81	13.84	−20.75	−20.63	5.03	5.00
11	28.88	28.89	−10.67	−10.65	5.03	5.00
16	44.56	44.50	−3.61	−3.58	5.03	5.00
21	44.56	44.50	−3.61	−3.58	−5.03	−5.00
26	28.88	28.89	−10.67	−10.65	−5.03	−5.00
31	13.81	13.84	−20.75	−20.63	−5.03	−5.00
36	1.12	1.14	−33.65	−33.38	−5.03	−5.00

Fig. 11. Cylindrical joint numerical test: (a) unloaded configuration; (b) final configuration.

under load case **2**, are compared to the corresponding NR outputs and summarized in Table 2.

5.3. Cylindrical joint

The aim of the following numerical test is to demonstrate the validity of the single-node cylindrical joint model introduced in Section 4.3.1.

Two rods (with length of 1m each) are joined together at their 'common' node by means of cylindrical joint, thus defining an overall 'L' shape with internal angle of 90°. Then, the first rod is clamped at its start node, while a vertical load $\overline{P}$ of 15 kN is applied at the end node of the second rod (see Fig. 11). Material and cross-sectional stiffnesses (E, G, A, I_x, I_y and J) are set in accordance to the previously described tests (subsections 5.1, 5.2) as well as the convergence criteria: $max \mid \overline{R}_i \mid \leqslant 9.5e - 6P$. Only two elements per rod are set.

Supposing, in first instance, to assume the rods elastic behavior as being infinitely stiff. Is such a case, the applied load would clearly not generate any rotation. In fact, both vector load $\overline{P}$ and the rotational axis of the cylindrical joint would remain aligned along the vertical direction (independently of the load's magnitude) thus, the system would rest in (initial) neutral equilibrium. On the other hand, assuming (as the case) finite stiffness values for the rods, the alignment between $\overline{P}$ and the rotational axis of the joint is lost as soon as the 1st rod starts twisting and bowing due to the effect of $\overline{P}$. Consequently, the (neutral) equilibrium is lost as well, and a rotation around the cylindrical joint is triggered to find a new (stable) equilibrium, which is eventually reached when: the 2nd rod's longitudinal axis, the joint rotational axis and the vector $\overline{P}$ are all aligned along the same vertical plane.

As shown in Fig. 11, at DR equilibrium convergence, the 2nd rod undergone a (local) counter-clockwise rotation of 0.325 rad (circa 18.6°) around the joint rotational axis.

5.4. Spherical dome

This example provides a description of the developed method with a practical application to the form finding and load analysis of a grid shell dome.

5.4.1. Form finding

The reference surface is described by the equation $f(\overline{r})$ of a sphere having radius of 11 m and its center coinciding with the global axes origin. The subspace of interest **B** is defined by $z \geqslant 4.582$ m so that each grid node whose z coordinate at time t is lower than such value, will not be constrained to the surface. Accordingly, the part of reference surface contained in **B** configures a spherical cap with a span of 20 m and circa 6.4 m high. The unstressed length L_0 of the two-way grid is set to 1 m. A flowchart of the form finding procedure is illustrated in Fig. 12: The mesh, obtained with the cutting method previously described, can be
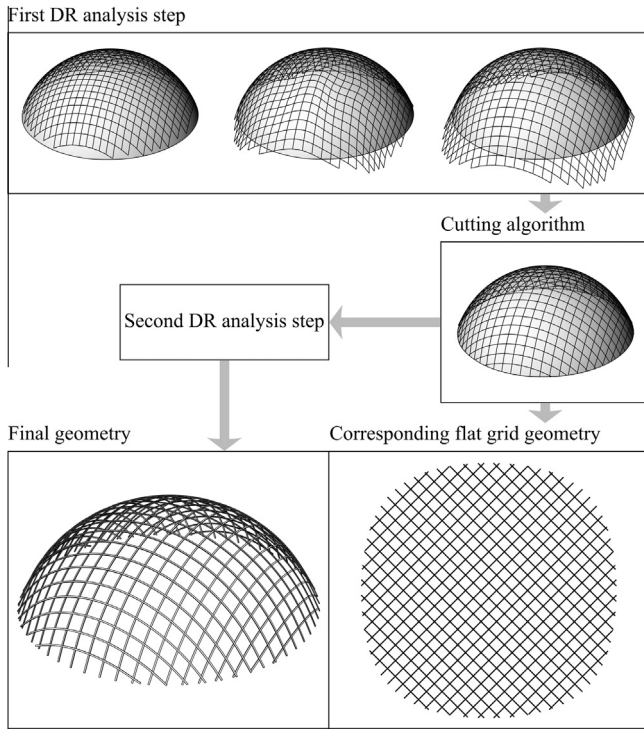
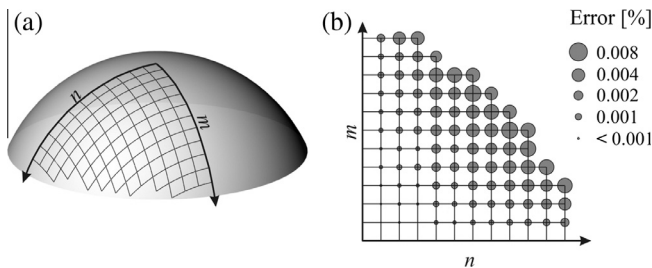**Fig. 12.** Form finding of a grid shell dome: flowchart.

Fig. 13. Spherical cap: (a) chebyshev net found by Eqs. (61) and (62); (b) comparison of DR output with the Chebyshev net geometry.

used to find the corresponding flat grid by 'relaxing' it on a flat surface. In fact, although geometrically different, the two meshes have the same topology. Unlike the single rod case, no analytical solution for a complete grid shell system is readily available to compare with the numerical solution. However, restricting the investigation to the assessment of the (global) grid node's displacements only for effect of the geometric constraints (constant elements length; reference surface) a comparison of outputs can be made with other discrete models. In the particular case of a spherical surface, the expression to calculate a corresponding discrete mesh with constant edge length (also called Chebyshev net) thus constant arch-length,[2] is given by Bobenko and Pinkall [37]: Assuming the nodes of the Chebyshev net defined by a $(n \times m)$ matrix, the unit vector $\bar{\omega}$ normal to the spherical surface at node $\bar{r}_{n+1,m+1}$ can be found from the unit vectors at nodes $\bar{r}_{n,m}$; $\bar{r}_{n+1,m}$ and $\bar{r}_{n,m+1}$ by:

$$\bar{\omega}_{n+1,m+1} = -\bar{\omega}_{n,m}$$
$$+ \frac{\bar{\omega}_{n,m} \cdot (\bar{\omega}_{n+1,m} + \bar{\omega}_{n,m+1})}{1 + (\bar{\omega}_{n+1,m} \cdot \bar{\omega}_{n,m+1})} (\bar{\omega}_{n+1,m} + \bar{\omega}_{n,m+1})$$
(61)

---

[2] To the case of spherical surface: for an arbitrary set of chords with constant length the corresponding geodesic arch-length is always constant.

Consequently, for a sphere with its center coinciding to the origin of the global coordinate system, the nodal coordinates are given by:

$$\bar{r}_{n+1,m+1} = (sphere\ radius)\bar{\omega}_{n+1,m+1}$$
(62)

On this basis, a Chebyshev net has been generated on a quarter of the spherical cap previously described, as shown in Fig. 13a. The nodes $\bar{r}_{n,0}$ and $\bar{r}_{0,m}$ of the first raw and column of the matrix are those obtained at completion of the first DR analysis step (grid still constrained to the surface) thus the remaining entries of the matrix are obtained by applying Eqs. (61) and (62). The error percentage is calculated as:

$$Error[\%] = \frac{100|\bar{r}^{DR} - \bar{r}^{Cheb.}|}{sphere\ radius}$$
(63)

As can be seen from Fig. 13b, the error increases with the distance from the axes of the matrix. Despite the arch-length of the Chebyshev net edges coinciding with the arch-length of the DR cubic splines at the $\bar{r}_{n,0}$ and $\bar{r}_{0,m}$ nodes, the discontinuity of tangents between consecutive Chebyshev net (geodesic) arches increases as we move away from the matrix axes. In any case, the discrepancy of outputs between the two geometries remains below the 0.01%.

5.4.2. Load analysis

The single-layer grid shell dome, obtained in the previous example, is submitted for a load analysis performed with both DR and NR methods, thus a comparison of results is provided. Material and cross-sectional stiffnesses are those set for the previously described tests. In order to take into account the effect of pre-stress forces for the NR analysis, a preliminary (form finding) analysis step is performed by imposing a set of displacements to the boundary nodes of the flat mat geometry (as shown in Fig. 14) where: both flat mat geometry and final position of the boundary nodes are those obtained by the DR procedure illustrated in Section 5.4.1. Further, for the NR analysis, the cylindrical joint connections are simulated by means of link elements, with a fictitious size of only 0.1 mm, in order to replicate the behavior of the single-node model adopted for the DR analysis.

For both DR and NR analyses, a gravitational load P is applied at each node of the structure by increments of 0.2 kN per node (up to 2 kN). For each load increment (load step) the equilibrium geometry is computed and the (average) vertical displacement, of the four nodes at the summit of the grid dome, is recorded. The equilibrium convergence criteria for the DR load steps is set to: $max\,|\,\bar{R}_i\,|\leqslant 0.005$ kN. The resulting load-displacement curves are reported in Fig. 16, according to which, the two analyses give very close results, with a maximum discrepancy < 1%. The deformed geometry for $P = 2$ kN per node obtained by DR method, is shown in Fig. 15 with a magnification factor of 30.

5.5. Corrugated barrel vault

In the present example, a reference surface is defined in such a way to replicate the overall shape of the Downland grid shell: The resulting corrugated barrel vault is 50 m long, with a varying width of 12.5–16 m, while the height varies from 9.5 m at the central hump to circa 7.4 m at the saddles [10]. According to the adopted surface function (see Appendix A), the global $(x,\ y)$ plane coincides with the ground floor level of the real structure whose longitudinal axis is directed along the y global direction. Hence, **B** is defined by: $(z \geqslant 0.0\ m)$ and $(-25.0\ m \leqslant y \leqslant 25.0\ m)$.

According to Harris et al. [5] the timber specimens were graded as D30 of the BS EN 338 [38] strength classification, for which a mean modulus of elasticity parallel to the grain $(E_{0,mean})$ of
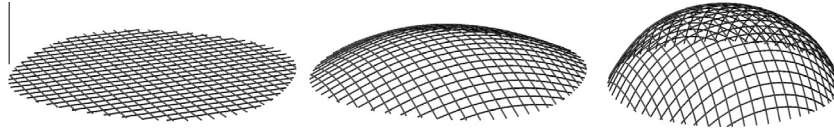
Fig. 14. Spherical cap: Preliminary form finding analysis by Newton–Raphson method. Grid cutting pattern and final position of the boundary nodes are those obtained at DR completion of the first form finding step.
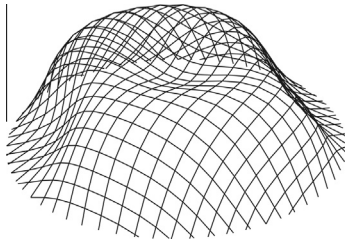

Fig. 15. Load analysis of the grid shell dome: deformed geometry obtained by DR method (scale – 30 times).
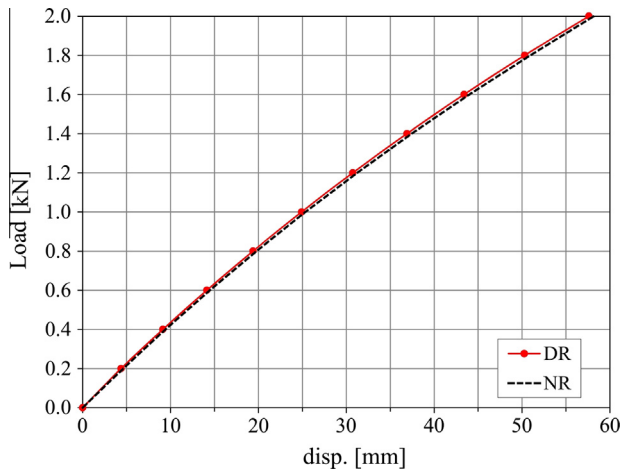

Fig. 16. Grid shell dome: load–displacement curves by DR and NR methods.

11 kN/mm^2 is given. Such value is estimated from tests on timber population at a temperature of 20 °C and relative humidity of 65%. In these environmental conditions, the *moisture content* (MC) of wood in general does not exceed 12% (dry timber) while the green oak used for the Downland grid shell construction had a corresponding MC up to 65% [5]. For values of MC over the *fiber saturation point* (around 27%) a reduction in stiffness and strength occurs. In order to take this into account, a E_{dry}/E_{green} ratio of 1.3 [39] is used to derive a 'reasonable' value of elastic modulus

$(E = E_{0,mean}/1.3 = 8.46$ kN/mm$^2)$ for input in Eqs. (20)–(24). A mean value of 0.69 kN mm^2 [38] is set for the transverse shear modulus *G*. The initial rectangular mat's overall shape [5] is preserved during the form finding analysis by constraining the vertical displacements of the boundary nodes of the mat's longer side. The grid shell geometry at form finding completion is shown in Fig. 17.

6. Conclusions

The work presented in this paper has aimed to facilitate the design of actively bent grid shells, with particular attention on the use of timber (see Fig. 18). A numerical framework is developed to address a range of issues at various design stages, including, a viable form finding procedure, structural analysis and assembly definitions (flat mat geometry) by combining finite element procedures (Dynamic Relaxation) with numerical methods typical of the computational geometry (mesh manipulation and geometry intersection). Further investigations, concerning the coupling of rotational degree of freedom, resulted in the development of a novel single-node numerical model for *large rotation* simulation of cylindrical joint systems. In addition, a procedure is illustrated to allow changing the element's cross-sectional properties during the completion of the form finding stage by maintaining the corresponding ends reactions values. Such procedure permits load analyses in which the increase in stiffness of the built-up timber ribs (for effect of shear blocks insertion) is taken into account, and at the same time maintains the equilibrium configuration (previously) obtained without shear blocks.

In order to allow the implementation of the described procedures, a detailed description of the equations involved is given. After preliminary validation tests on 'simple' structural systems, the procedures are applied to the form finding, structural analysis and mat cutting patterns search of a grid shell dome, as well as the form finding analysis of a corrugated barrel vault.

The accompanying numerical tests demonstrated the reliability of the proposed method. The preliminary tests showed a good level of accuracy for the six DoF DR formulation in the estimation of the load-displacements functions. Accordingly, the six DoF DR can be used for non-linear buckling analyses at the completion of the form finding routine (by adding a non-null term $\overline{P}_i$ to the residuals: Eq. (3)) thus allowing to take into account the effect of pre-stress (and material relaxation) on the final load bearing capacity.
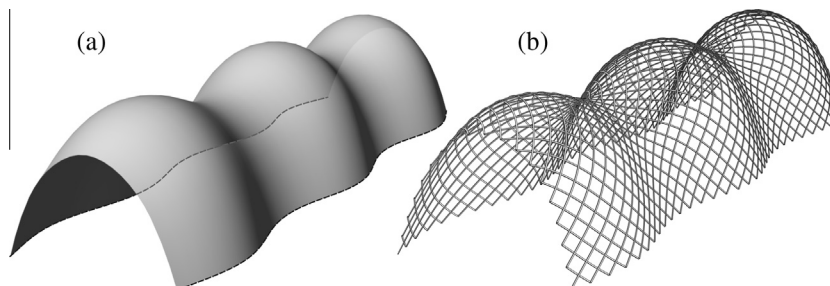

Fig. 17. Corrugated barrel vault: (a) reference surface; (b) final geometry.

Fig. 18. Post-formed timber grid shells [16].

Appendix A. Barrel vault shape function

As in [40] the vertical z component of the reference surface is obtained by superposition of multiple function values. Writing $f(\bar{r}) = f(x,y,z) = 0$ in the form $f(x,y) = z$, we have:

$$z = f = f_1 + f_2 + f_3 + c \tag{A.1}$$

where

$$f_1 = -\cosh\left(\frac{x}{2.55}\right); \quad f_2 = \cosh\left(\frac{x}{4.1}\right)\cos\left(\frac{y}{3}\right)$$
$$f_3 = -\left(\frac{x^2}{50} + \frac{y^2}{665}\right); \quad c = 9.55 \tag{A.2}$$
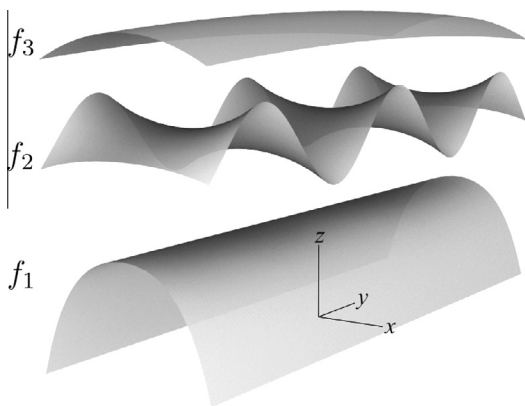

Fig. A.1. Corrugated barrel vault: $f(\bar{r}) = f_1 + f_2 + f_3 + c$.

The main barrel vault is shaped with f_1 while f_2 provides the corrugated profile and f_3 takes into account the occurring height difference between the central dome and the lateral ones (see Fig. A.1) the constant c translates vertically the surface so that the global (x, y) plane coincides to the structure's ground floor.

From Eqs. (A.2) the partial derivatives of $f(\bar{r})$ to insert in Eq. (53) to compute the vector normal to the surface, result to be:

$$\frac{\partial f}{\partial x} = -\frac{1}{2.55}\sinh\left(\frac{x}{2.55}\right) + \frac{1}{4.1}\sinh\left(\frac{x}{4.1}\right)\cos\left(\frac{y}{3}\right) - \frac{x}{25}$$
$$\frac{\partial f}{\partial y} = -\frac{1}{3}\cosh\left(\frac{x}{4.1}\right)\sin\left(\frac{y}{3}\right) - \frac{y}{332.5} \tag{A.3}$$
$$\frac{\partial f}{\partial z} = -1$$

References

[1] Harris R. Design of timber gridded shell structures. Proc ICE-Struct Build 2011;164(2):105–16. http://dx.doi.org/10.1680/stbu.9.00088.
[2] Pirazzi C, Weinand Y et al. Geodesic lines on free-form surfaces: optimized grids for timber rib shells. In: Proc world conference on timber engineering, vol. 7; 2006.
[3] Natterer J, Burger N, Müller A. Das expo-dach in hannover als pilotprojekt für den holzbau-entwicklung und einsatz nicht geregelter bauweisen. Bautechnik 2001;78(10):693–705. http://dx.doi.org/10.1002/bate.200104840.
[4] Happold E, Liddell W. Timber lattice roof for the mannheim bundesgartenschau. Struct Eng 1975;53(3):99–135.
[5] Harris R, Romer J, Kelly O, Johnson S. Design and construction of the downland gridshell. Build Res Inform 2003;31(6):427–54. http://dx.doi.org/10.1080/0961321032000088007.
[6] Harris R, Haskins S, Roynon J. The Savill garden gridshell: design and construction. Struct Eng 2008;86(17):27–34.
[7] Pone S, D'Amico B, Colabella S, Parenti B, Lancia D, Fiore A, et al. Construction and form-finding of a post-formed timber grid-shell. In: Structures and architecture. Concepts, applications and challenges; 2013. p. 245–52. http://dx.doi.org/10.1201/b15267-32.
[8] D'Amico B, Kermani A, Zhang H. A form finding tool for post formed timber grid shells. In: Proceedings of the world conference on timber engineering, Quebec City, Canada; 2014. http://dx.doi.org/10.13140/2.1.3949.8888.
[9] Lienhard J, Alpermann H, Gengnagel C, Knippers J. Active bending, a review on structures where bending is used as a self-formation process. Int J Space Struct 2013;28(3):187–96. http://dx.doi.org/10.1260/0266-3511.28.3-4.187.

[10] Kelly O, Harris R, Dickson M, Rowe J. The construction of the downland gridshell. Struct Eng 2001;79(17):25–33.

[11] Douthe C, Baverel O, Caron J-F. Form-finding of a grid shell in composite materials. J Int Assoc Shell Spatial Struct 2006;150:53.

[12] Bouhaya L, Baverel O, Caron J-F. Optimization of gridshell bar orientation using a simplified genetic approach. Struct Multidiscip Optim. http://dx.doi.org/10.1007/s00158-014-1088-9.

[13] Bouhaya L, Baverel O, Caron J-F. Mapping two-way continuous elastic grid on an imposed surface: application to grid shells. In: Proc 50th IASS symposium, Valencia, Editorial de la Universitat Politécnica de Valencia; 2010.

[14] Li J-M, Knippers J. Form-finding of grid shells with continuous elastic rods. In: Proc of the IABSE-IASS symposium, London, UK, vol. 35; 2011.

[15] Kuijvenhoven M, Hoogenboom P. Particle-spring method for form finding grid shell structures consisting of flexible members. J Int Assoc Shell Spatial Struct 2012;53(1):31–8.

[16] Pone S, Colabella S, D'Amico B, Lancia D, Fiore A, Parenti B. Timber post-formed gridshell: digital form-finding/drawing and building tool. In: Proc of the IASS symposium, Wroclaw, Poland; 2013.

[17] Harris R, Gusinde B, Roynon J. Design and construction of the pods sports academy, Scunthorpe, England. In: Proceedins of the world conference on timber engineering; 2012. p. 510–7.

[18] Hernandez EL, Sechelmann S, Rörig T, Gengnagel C. Topology optimisation of regular and irregular elastic gridshells by means of a non-linear variational method. In: Advances in architectural geometry 2012. Springer; 2013. p. 147–60. http://dx.doi.org/10.1007/978-3-7091-1251-9_11.

[19] Cundall PA. Explicit finite difference methods in geomechanics. In: Proc. of the EF conference on numerical methods in geomechanics, Blacksburg, Virginia, vol. 1; 1976. p. 132–50.

[20] Day A. An introduction to dynamic relaxation. Engineer 1965;219:218–21.

[21] Otter JRH, Cassell AC, Hobbs RE, et al. Dynamic relaxation. ICE proceedings, vol. 35. Thomas Telford; 1966. p. 633–56.

[22] Topping B, Khan A. Parallel computation schemes for dynamic relaxation. Eng Comput 1994;11(6):513–48. http://dx.doi.org/10.1108/02644409410799407.

[23] Barnes MR. Form finding and analysis of tension structures by dynamic relaxation. Int J Space Struct 1999;14(2):89–104. http://dx.doi.org/10.1260/0266351991494722.

[24] Lewis WJ. Tension structures: form and behaviour. Thomas Telford; 2003. http://dx.doi.org/10.1680/tsfab.32361.

[25] Adriaenssens S, Barnes M. Tensegrity spline beam and grid shell structures. Eng Struct 2001;23(1):29–36. http://dx.doi.org/10.1016/S0141-0296(00)00019-5.

[26] Barnes MR, Adriaenssens S, Krupka M. A novel torsion/bending element for dynamic relaxation modeling. Comput Struct 2013;119:60–7. http://dx.doi.org/10.1016/j.compstruc.2012.12.027.

[27] Wakefield D. Dynamic relaxation analysis of pre-tensioned networks supported by compression arches. PhD thesis. City University, London; 1980.

[28] Ong CF. Computer aided design of tension structures. PhD thesis. City University, London; 1992.

[29] Adriaenssens SML. Stressed spline structures. PhD thesis. University of Bath; 2000.

[30] Tuckerman M, Berne BJ, Martyna GJ. Reversible multiple time scale molecular dynamics. J Chem Phys 1992;97(3):1990–2001. http://dx.doi.org/10.1063/1.463137.

[31] Papadrakakis M. A method for the automatic evaluation of the dynamic relaxation parameters. Comput Methods Appl Mech Eng 1981;25(1):35–48. http://dx.doi.org/10.1016/0045-7825(81)90066-9.

[32] Rodrigues O. De l'attraction des sphéroïdes. PhD thesis; 1815.

[33] Aharonov Y, Farach HA, Poole Jr CP. Nonlinear vector product to describe rotations. Am J Phys 1977;45(5):451–4. http://dx.doi.org/10.1119/1.10835.

[34] Harris R, Johnson S, Holloway A, Zeuner C. A coupling and a method of constructing grid shell buildings using such a coupling. Patent GB2361504 (A) (10 2001).

[35] Williams CJ. Patterns on a surface: the reconciliation of the circle and the square. Nexus Network J 2011;13(2):281–95. http://dx.doi.org/10.1007/s00004-011-0068-2.

[36] Timoshenko SP, Gere JM. Theory of elastic stability. McGraw-Hill; 1961.

[37] Bobenko A, Pinkall U. Discrete surfaces with constant negative gaussian curvature and the hirota equation. J Differ Geom 1996;43(3):527–621.

[38] BS EN 338:2009. Structural timber – strength classes. British Standards Institution.

[39] ASTM D2555-06. Standard practice for establishing clear wood strength values. American Society for Testing and Materials; 2006.

[40] Williams CJK. The analytic and numerical definition of the geometry of the british museum great court roof. In: Mathematics & design 2001. Deakin University; 2001. p. 434–40.